Orientation Dependent Interlayer Stacking Structure in Bilayer MoS_2 domains

Shanshan Wang[1], Hidetaka Sawada[1,2,3], Christopher S. Allen[1,3], Angus I. Kirkland[1,3], Jamie H. Warner[1]*

[1]Department of Materials, University of Oxford, Parks Road, Oxford, OX1 3PH, United Kingdom

[2]JEOL Ltd., 3-1-2 Musashino, Akishima, Tokyo 196-8558, Japan

[3]Electron Physical Sciences Imaging Center, Diamond Light Source Ltd, Didcot, Oxfordshire, OX11 0DE, United Kingdom

*Jamie.warner@materials.ox.ac.uk;

Abstract

We have studied the atomic structure of small secondary domains that nucleate on monolayer MoS_2 grown by chemical vapour deposition (CVD), which form the basis of bilayer MoS_2. The small secondary bilayer domains have a faceted geometry with three-fold symmetry and adopt two distinct orientations with 60^o rotation relative to an underlying monolayer MoS_2 single crystal sheet. The two distinct orientations are associated with the 2H and 3R stacking configuration for bilayer MoS_2. Atomic resolution images have been recorded using high angle annular dark field scanning transmission electron microscopy (HAADF-STEM) that show the edge termination, lattice orientation and stacking sequence of the bilayer domains relative to the underlying monolayer MoS_2. These results provide important insights that bilayer MoS_2 growth from 60^o rotated small nuclei on the surface of monolayer MoS_2 could lead to defective boundaries when merged to forming larger continuous bilayer regions and that pure AA' or AB bilayer stacking may be challenging unless from a single seed.

KEYWORDS: MoS_2, HAADF-STEM, 2D materials, bilayers

Layered molybdenum disulphide (MoS_2) has recently attracted interest due to its direct bandgap in single layer form, which exhibits semiconducting performance and expands the potential application of 2D materials in nanoelectronics and optoelectronics.[1–4] Monolayer MoS_2 has Mo atoms bonded to S atoms in a trigonal prismatic coordination by strong covalent bonds, while the interactions between layers are due to weak van der Waals (vdW) forces. This layered configuration gives rise to polytypism in few-layer MoS_2 with different stacking structures. A change in MoS_2 from monolayer to bilayer modifies the band structure, providing tunability in electrical, optical, vibrational and chemical properties.[5–8] It has been reported that few-layer MoS_2 shows higher carrier mobility,[9,10] better chemical stability[11,12] and a more sensitive field-induced effect[13,14] in transistors than its monolayer counterpart. Moreover, the bandgap of bilayer MoS_2 can be tuned by applying a vertical electric field.[15] For these reasons, few-layer MoS_2 is a good candidate for valley-tronics due to the degree of freedom offered by additional layers.[16,17]

The stacking order between adjacent MoS_2 layers has been shown to be one of the major factors that influence the properties of few-layer MoS_2 properties in several experimental and theoretical studies. Different stacking sequences modify the crystal symmetry, which varies the Coulomb interaction between layers resulting in different equilibrium interlayer distances.[5,18] Therefore, many physical properties of 2D layered materials including bandgap size, phonon vibration frequency, magnetism and superconductivity can be manipulated by altering the layer stacking configuration.[19,20] The most energetically favourable polytypes of few-layer MoS_2 are 2H (space group: $P6_3/mmc$) and 3R (space group: $R3m$) (Figure 1a), which have the same intralayer coordination (trigonal prismatic coordination between the Mo and adjacent S atoms) but with different interlayer stacking.[21]

Fabricating few-layer MoS_2 with specific stacking order can be achieved by two main routes: (i) sequential mechanically stacking of MoS_2 monolayers with a precise control over twist angles;[22]

(ii) growth of few-layer MoS_2 followed by a selection of quantified stacking sequences.[18,19,23] Direct growth of few-layer MoS_2 crystals has the advantage of scalable production and no interlayer contamination and in particular, chemical vapour deposition (CVD) growth of MoS_2 has been achieved with wafer scale coverage.[24–27] CVD growth of monolayer MoS_2 is often carried out using amorphous substrates such as SiO_2/Si wafers, whereas the second layer of MoS_2 grows on the crystalline monolayer MoS_2 surface. Compared to the intensive study of monolayer MoS_2, research on the growth of few-layer MoS_2 and corresponding structural analysis is limited.

In addition to stacking sequences, the edge is another significant structural parameter that can influence the electrical, optical, magnetic and catalytic properties of 2D materials. Fabricating specific edge structures in graphene nanoribbons can open up a band gap and create unique spin states under the influence of an electric field.[28,29] Moreover, study on edges facilitates an in-depth understanding of growth mechanisms at the atomic scale and can help correlate the synthesis (precursor concentration, substrate, *etc.*) with the resultant 2D material structure.[30,31] There have also been several theoretical reports relating the edge structure of MoS_2 to its properties,[32–34] including the prediction of a ferromagnetic ground state for Mo-terminated edges as well as metallic and semiconducting behaviour in zigzag and armchair MoS_2 nanoribbons.[35] Experimentally, aberration-corrected transmission electron microscopy (AC-TEM) in phase contrast imaging mode and scanning transmission electron microscopy (AC-STEM) can determine edge structures.[36–39] High angle annular dark field STEM (HAADF-STEM) is particularly suitable for structural studies of 2D multi-element materials, such as MoS_2, due to its z-dependent contrast.[40,41] Mo- and S-zigzag edges are most commonly observed in as-grown monolayer MoS_2, with several reconstructed configurations having been observed with different S coverage or displacements in the outermost atomic rows.[39] The structure and evolution of torn edges as the defect concentration increases in cracked monolayer MoS_2 samples have also been investigated.[42]

Here we use aberration corrected HAADF-STEM to study the atomic structure of smaller secondary domains of MoS_2 that nucleate on top of a larger underlying monolayer single crystal grown by CVD. We examine the crystal shape, stacking order and the step edge configurations of the MoS_2 secondary domains relative to the underlying larger MoS_2 monolayer. The MoS_2 secondary layers mostly adopt a three-pointed geometry, similar to a shuriken and are epitaxially matched to the MoS_2 monolayers in both 2H and 3R phases. The atomic configurations on step edges for differently stacked second layers are various, with 50% S-covered Mo Klein edges for 2H stacking and Mo-terminated zigzag edges for 3R stacking. The growth mechanism for these epitaxially stacked shuriken shaped MoS_2 second layers are also investigated, indicating the kinetic controlled growth conditions and a substrate influence from the bottom crystalline MoS_2 monolayer.

Results and discussion

For bilayer MoS_2, there are five possible high-symmetry stacking sequences, denoted as AA, AA', AB, AB' and A'B, consistent with the nomenclature for bilayer hexagonal boron nitride (*h*-BN).[5,43] The 2H and 3R polytypes of MoS_2 bilayers correspond to AA' and AB stacking (Figure 1a), which are the most energetically stable and commonly observed phases in natural and synthetic materials. For AA' stacking, the Mo (S) atoms in one layer overlap with the S (Mo) atoms in the other layer. The lattice orientation between the two layers is rotated by 60° with all atoms in the two layers fully eclipsed. AB stacking consists of two staggered layers with 0° rotation, where double stacked S atoms in one layer are located above (below) the centers of the hexagonal rings in the other layer. In this configuration three different atomic columns are observed in the top down projection; a single Mo atom, two S atoms plus one Mo atom, and two S atoms, respectively, marked as 1', 2' and 3' in Figure 1a. These two stacking sequences can be interconverted through rotation around an axis, perpendicular to the sheet as shown in Figure 1c.

Figure 1b shows an HAADF-STEM image of several smaller MoS_2 domains on the surface of a larger single crystalline monolayer. The small 2nd layer nuclei have a triangular geometry, as indicated by green dashed circles, while the larger ones have a three-pointed shuriken-like shape. The larger secondary domains align along two different orientations with a 60° rotation, which are identified by three tips of each domain and labelled by yellow and red markers, respectively. Mo zigzag and S zigzag structures have been reported as the two most energetically favourable edge terminations in monolayer MoS_2,[44] and we therefore propose two alternative structures that could lead to the generation of these two types of larger 2nd-layer domains as shown in Figure 1d. We suggest that either the domains arise from different sub-lattice sites with the same 2nd-layer lattice orientation, in which case one triangle is S zig-zag edge terminated and the other is Mo zig-zag edge terminated (left panel of Figure 1d) (leading to AA' and AB' stacking), or that they adopt different 2nd-layer lattice orientations, with a 60° rotation, in which case both have the same Mo zig-zag sub-lattice edge terminations (right panel of Figure 1d) (leading to AA' and AB stacking).

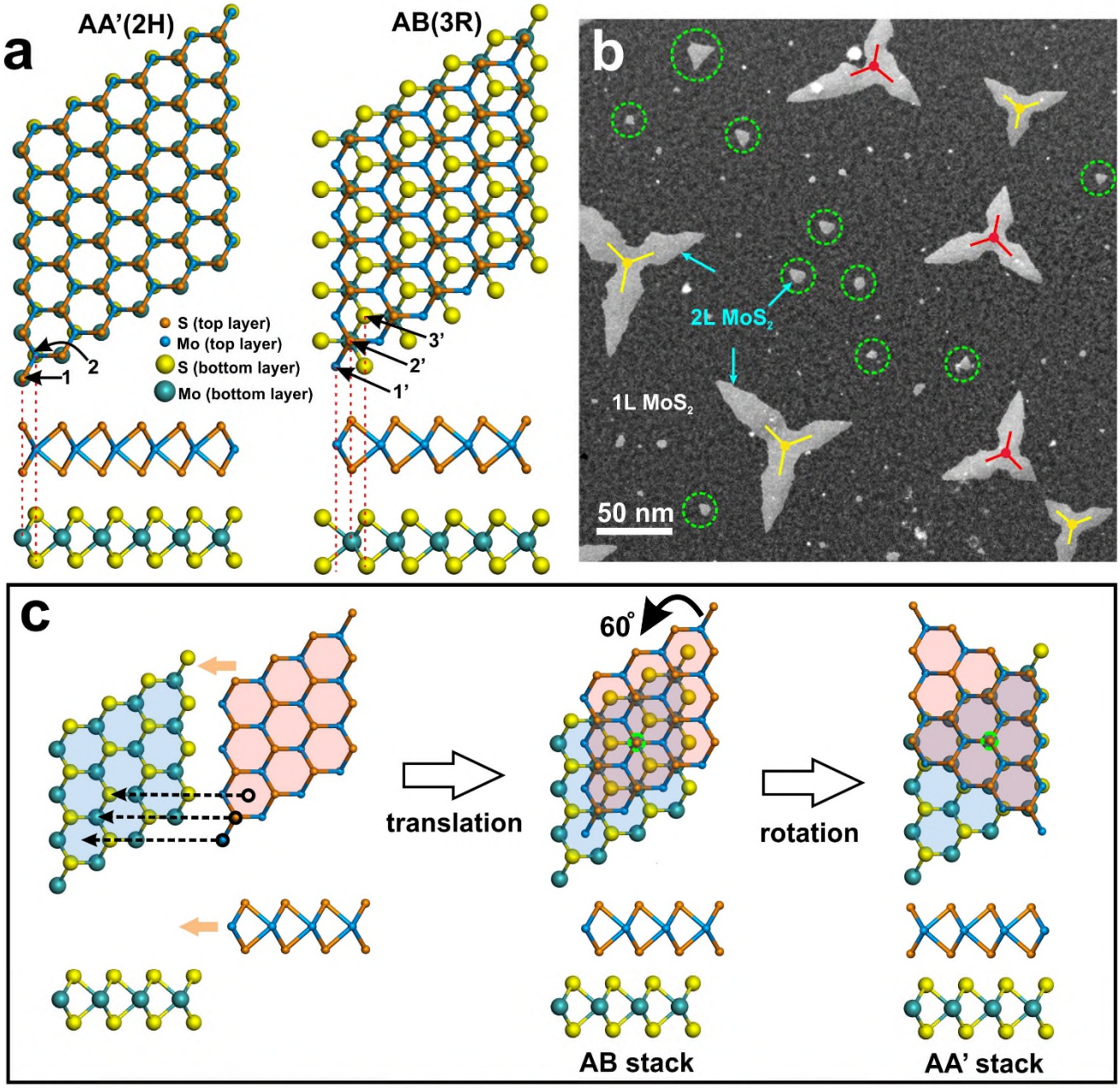
a
AA'(2H)
AB(3R)
S (top layer)
Mo (top layer)
S (bottom layer)
Mo (bottom layer)
1
2
1'
2'
3'
b
2L MoS2
1L MoS2
50 nm
c
60°
translation
rotation
AB stack
AA' stack
d
Mo-terminated zigzag edge
S-terminated zigzag edge
Layer 1
Layer 2
Mo-terminated zigzag edge
60°
Layer 2
Layer 2

Figure 1. (a) Schematic illustration of 2H and 3R polytypes in MoS_2 bilayers, corresponding to AA' and AB stacking sequences. Orange, blue, yellow and green spheres in the atomic model indicate S atoms in the top MoS_2 layer, Mo atoms in the top MoS_2 layer, S atoms in the bottom MoS_2 layer and Mo atoms in the bottom MoS_2 layer, respectively. (b) Low magnification HAADF-STEM image showing three-pointed shuriken-shaped MoS_2 bilayers on single-crystalline monolayer MoS_2 in two different epitaxial orientations with a 60° rotation. Domains with two different stacking sequences are labelled by yellow and red marks, respectively. There are also distributions of small nuclei in the vicinity of the larger domains, indicated by green dashed circles. (c) Schematic diagram showing the transformation between AB and AA' stacking. The top and bottom MoS_2 monolayer are indicated by a red and a blue background, respectively, so that the stacked bilayer region can be visualised as a color difference. The center of the 60° rotation from the AB to the AA' sequence is marked by a green dashed circle. (d) Schematic illustration showing two possible structural relationships between two larger 2^{nd}-layer MoS_2 domains rotated by 60°. The red background represents the 1^{st}-layer of the underlying single-crystalline MoS_2 film.

Figure 2a shows the tip region of a 2^{nd}-layer MoS_2 crystal (highlighted by a yellow box inset) corresponding to the shuriken-shaped domain outlined by a dashed red triangle in Figure 1b. An obvious contrast difference can be seen between the bilayer and the monolayer region. The slight contrast non-uniformity across the HAADF-STEM image originates from residual hydrocarbon contamination absorbed on the specimen. The tip of the domain is not atomically sharp and also shows uneven edges. Figure 2b shows an extended step edge of the 2^{nd}-layer MoS_2, corresponding to the region indicated by the blue arrow in the inset to Figure 2a together with the power spectrum calculated from Figure 2b with white circles indicating {100} reflections (zigzag lattice orientation) and green circles corresponding to {110} reflections (armchair lattice orientation). The HAADF image and its corresponding power spectrum indicate that the long 2^{nd}-layer step edge predominantly aligns along the zigzag lattice direction with occasional deflections and small terraces. Figure 2c shows a magnified image taken from the region marked with a white box in Figure 2a with the corresponding atomic model and multislice HAADF image simulation shown in Figures 2d and 2e, respectively. Intensity

line profiles across two adjacent lattice rows through the 2nd-layer MoS_2 step edge, labelled by 1 and 2 in Figure 2c and 2e, are measured for both experimental and simulated HAADF images, showing a good agreement (Figure 2f and 2g). The HAADF-STEM image indicates that this bilayer region exhibits AA' stacking. Most step edges of AA' stacked 2nd-layer MoS_2 adopt the 50% S-covered Mo Klein edge structure with single dangling S atoms at Mo-terminated zigzag edges, as shown in Figure 2d. The attachment of these single S atoms to edges is also supported by the intensity line profiles in Figure 2f, highlighted by the blue arrow (Figure S1). We also observed a small background intensity fluctuation in the monolayer region close to the 2nd-layer step edge in the experimental HAADF-STEM image, as shown by the black dashed lines in Figure 2f which could be attributed to residual C contamination.

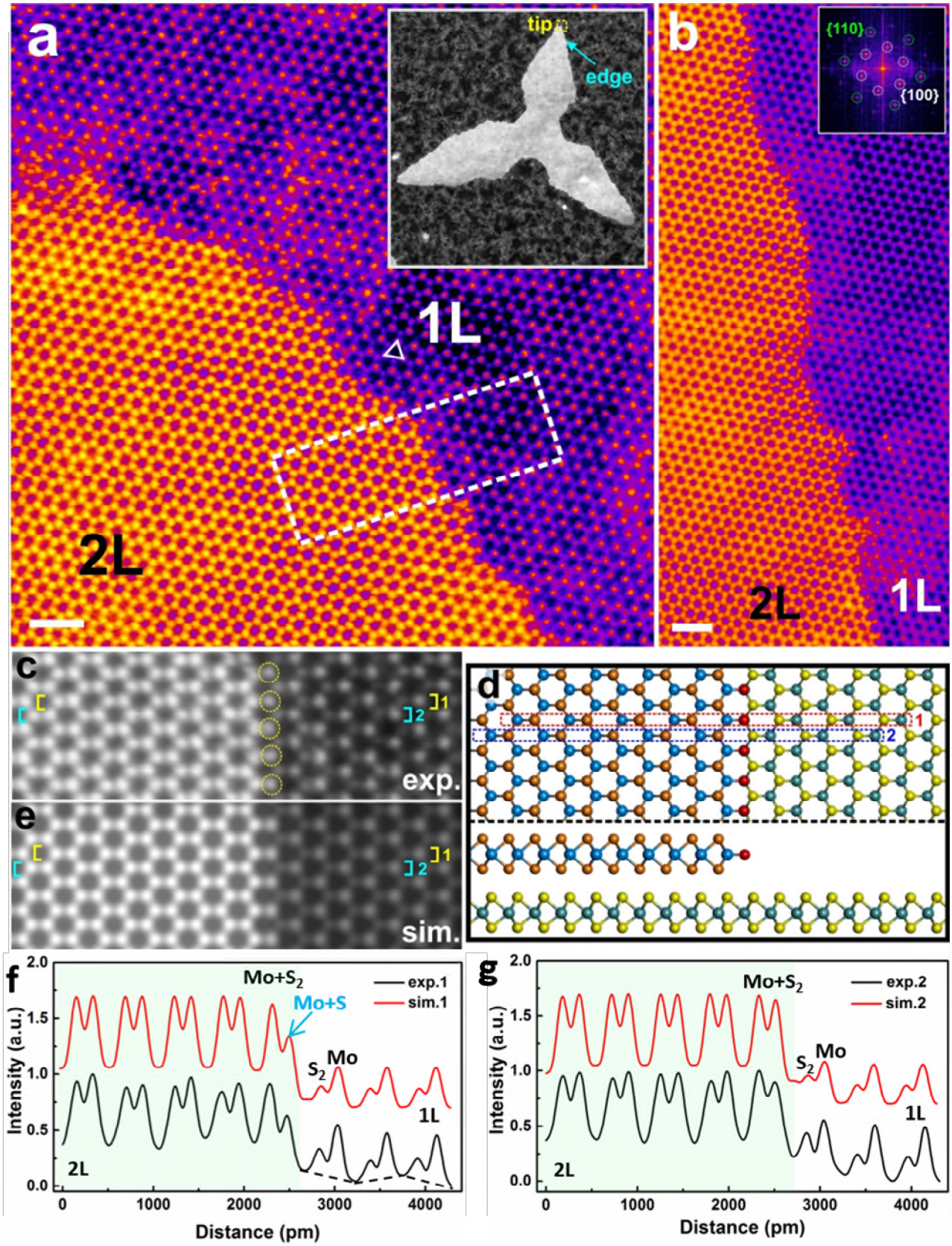

Figure 2. HAADF-STEM image showing the 2nd-layer step edge configuration of AA' stacked bilayer MoS_2. (a) HAADF-STEM image of the tip region of AA' stacked 2nd-layer MoS_2, corresponding to the area

marked by the yellow box in the inset. The lattice orientation of the 1st-layer MoS_2 is indicated by the small white triangle. (b) HAADF-STEM image showing the extended 2nd-layer MoS_2 step edge, corresponding to the region indicated by the cyan arrow in the inset to (a). Power spectrum calculated from (b) is shown inset. (c) Magnified image of the white-boxed region in (a). (d) Atomic model based on (c) showing both projection and side views. Single S atoms at the Mo-terminated zigzag edge of the 2nd-layer MoS_2 are highlighted in red. (e) Multislice HAADF-STEM image simulation corresponding to the atomic model in (d) (see simulation parameters in Methods). (f) Intensity line profiles measured from the selected area labelled 1 (yellow square brackets) in (c) and (e), respectively. The structure corresponds to the region marked by the red dashed box in (d). (g) Intensity line profiles measured from the selected area labelled 2 (cyan square brackets) in (c) and (e), respectively. The structure corresponds to the region marked by the blue dashed box in (d). Green shading in both (f) and (g) indicates the region of 2nd-layer MoS_2. All scale bars correspond to 1nm.

Figure 3a shows the step edge of the other type of orientated three-pointed shuriken-shaped 2nd-layer MoS_2, corresponding to domains outlined by the yellow dashed triangle in Figure 1b, which are rotated by 60° with respect to the 2nd-layer MoS_2 domain shown in the inset of Figure 2a. The lattice direction for the 1st-layer MoS_2 in Figure 3a is the same as that in Figure 2a, as indicated by the small yellow and white triangles in the corresponding images. This confirms the single crystalline nature of the bottom 1st-layer MoS_2. The step edge is parallel to the zigzag direction with small terraces. Figure 3b shows the domain tip geometry, which has a truncated cusp consisting of three sides oriented by 120°. All three edges at the tip are aligned to three zigzag directions of the MoS_2 lattice. Figure 3c shows a magnified HAADF-STEM image of the region defined by the orange box in Figure 3a with corresponding atomic models and multislice HAADF simulation shown in Figure 3d and 3e, respectively. Intensity line profiles along the armchair lattice direction across the 2nd-layer step edge in both experimental and simulated HAADF images are shown in Figure 3f and 3g, which shows three different atomic columns with different contrast. These are assigned as 2S, Mo and 2S+Mo from the lowest to the highest contrast, respectively. In addition, orientation of the two layers is staggered, with atoms observed in the hollow centers of hexagonal rings in projection consistent with AB stacking.

The 2nd-layer step edge adopts the Mo-terminated zigzag configuration, which aligns with the same lattice direction as the 50% S-covered Mo Klein edge observed in the AA' stacked 2nd-layer MoS_2 but without dangling S atoms in the outermost row.

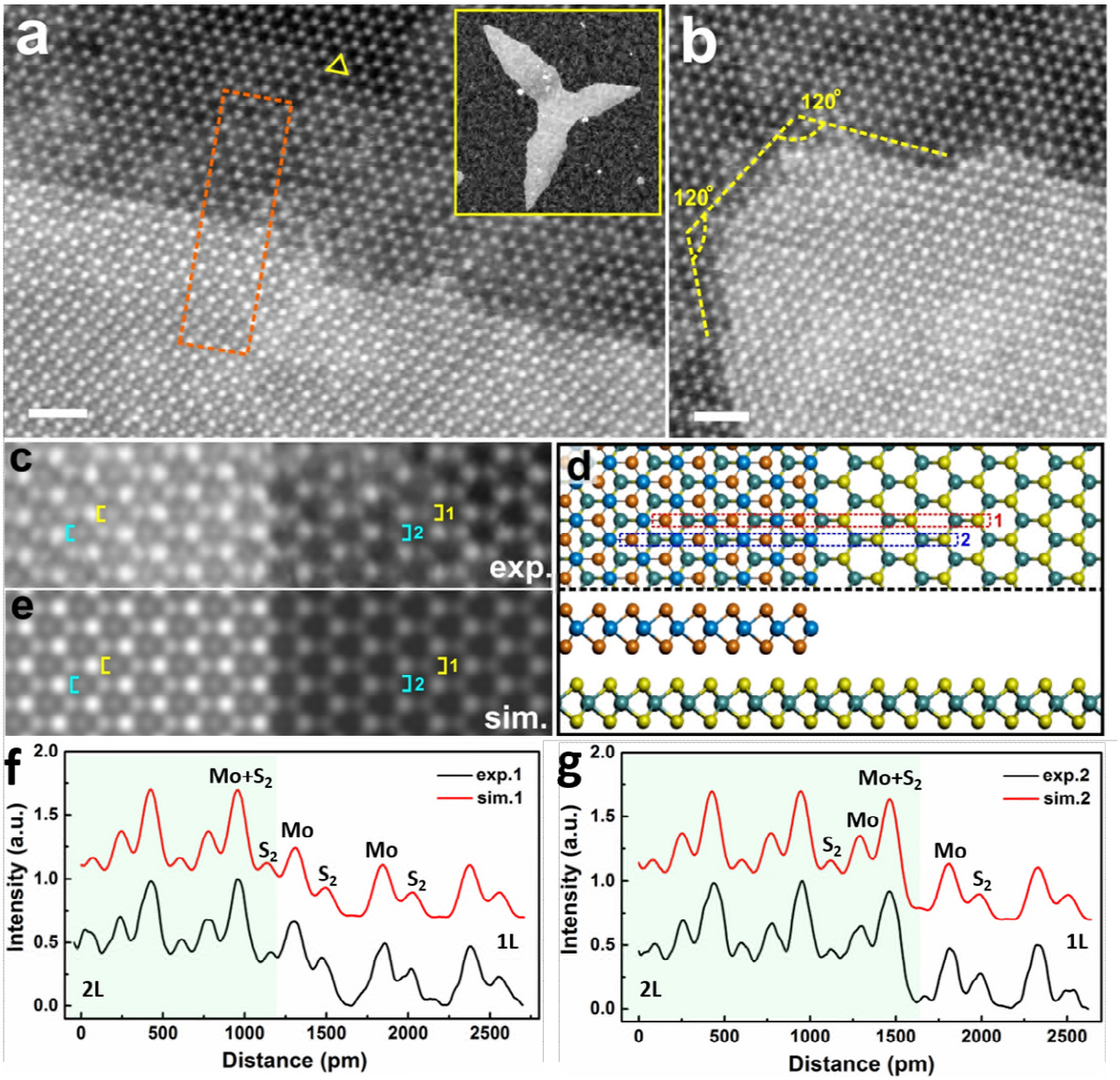

Figure 3. HAADF-STEM image showing the 2nd-layer step edge configuration of AB stacked bilayer MoS_2. (a) HAADF-STEM image showing AB stacked 2nd-layer MoS_2. The lattice orientation of the 1st-layer MoS_2 is marked by the yellow triangle in the same direction as the 1st-layer MoS_2 in Figure 2a. Inset is a low-magnification image showing the domain orientation of the 2nd-layer MoS_2 in the AB stacking sequence, which

is rotated by 60° with respect to the AA' stacked 2nd-layer domain shown inset to Figure 2a. (b) ADF-STEM image of the tip region of the 2nd-layer MoS_2. (c) Magnified image of the orange boxed area in (a). (d) Atomic model based on (c) showing both projection and side views. (e) Multislice HAADF-STEM image simulation corresponding to the atomic model in (d) (see simulation parameters in Methods). (f) Intensity line profiles measured from the area labelled 1 (yellow squared brackets) in (c) and (e), respectively. The structure corresponds to the region marked by the red dashed box in (d). (g) Intensity line profiles measured from the selected area labelled by 2 (cyan square brackets) in (c) and (e), respectively. The structure corresponds to the region marked by the blue dashed box in (d). Green shading in both (f) and (g) indicates the region of 2nd-layer MoS_2. All scale bars correspond to 1nm.

In Figure 4b, we show the relative occurrence of AA' and AB stacking in bilayer MoS_2, taking into account both the large shuriken-shaped domains and the small triangular nuclei. All of the shuriken-shaped domains and smaller triangular nuclei with defined size and shape obey either AA' or AB stacking sequences indicating an energetic advantage for these two stacking configurations under the growth conditions used. The ratio between AA' and AB stacked domains is almost equal at 45% and 55%, respectively, when considering both shuriken and triangular domains (Figure S2). It was observed that smaller nuclei are distributed in regions that are not close to larger shuriken-shaped domains, leaving a depletion area around each shuriken-shaped domain with a relatively low concentration of smaller nuclei (Figure 1b). It is also observed that, for closely situated pairs of shuriken-shaped domains with tips grown towards each other, the tips from two domains that grow head to head are shorter than the other tips in the same domain (Figure 4c–f). These two phenomena indicate that our shuriken-shaped 2nd-layer MoS_2 were grown in conditions where the surface migration distance of active precursor species on the monolayer MoS_2 substrate is the governing factor. This growth condition also can explain the formation of the shuriken geometry for 2nd-layer MoS_2. It is known that the surface curvature of crystal nuclei or liquid droplets could influence the speed of mass transfer, such as the crystal growth and the droplet evaporation, based on the Kelvin equation.[47] For instance, in the crystal aging process, small nuclei with a convex surface and a higher surface

curvature will spontaneously transfer their substances to larger crystals with a flatter surface and a lower surface curvature in the mother solution, resulting in the disappearance of small nuclei and the achievement of large crystals with more uniform sizes eventually. This can be explained by an increase of the surface energy with increasing degree of surface curvature. However, our case is opposite to the example above, as the tip with a larger convex surface curvature in a triangular 2nd-layer MoS_2 nucleus grows faster than the side, leading to formation of shuriken-shaped large crystals. This can be interpreted by a simple kinetic model illustrated in Figure 4g. As the growth is kinetically controlled by the transfer ability of precursor species, we can assume the longest migration distance of the precursor species absorbed on the 1st-layer MoS_2 under this synthesis condition as '*d*', meaning that only those precursor species locating within the distance of '*d*' from the edges of a 2nd-layer MoS_2 nucleus can move and attach to the nucleus. Then, we can select two points on the domain tip and side, respectively, and mark corresponding two regions where precursor feedstocks can effectively reach the 2nd-layer MoS_2 edges, as indicated by the yellow and green areas on the left blue triangle in Figure 4g. It is clear that the point on the domain tip with a higher convex surface curvature obtains a larger sector region of precursor supplements than the point on the flat domain side, leading to a faster growth rate of the tip and finally resulting in the crystal geometry with extended tips for the 2nd-layer MoS_2. When two nuclei situated close together with two tips growing along the same axis in opposite directions, the regions of precursor supplements at two tips could overlap (yellow and red regions in Figure 4g), leading to a competition for the precursor species between them. This results in less precursor supply to these two tips compared to others, causing slower growth rate and eventually shorter tip lengths. The other geometric feature of note in the shuriken-shaped domains is the specific side curvature, as shown by the yellow dashed lines along the domain boundaries in Figure 4c and 4d. This boundary has several sharp deflections close to 120° and differentiates the shuriken-shaped second layers from the previously observed three-pointed star-shaped monolayer MoS_2 grown on amorphous SiO_2/Si substrates,[31,48]. This shape could also be rationalised by the effect of growth on a

crystalline 1st-layer MoS_2. Since step edges along certain lattice directions (e.g. the Mo zigzag direction) might have a lower total energy, the 2nd-layer domains contain several sharp deflections with angles that sustain the preferable step edge orientations (e.g. 60°, 120°).

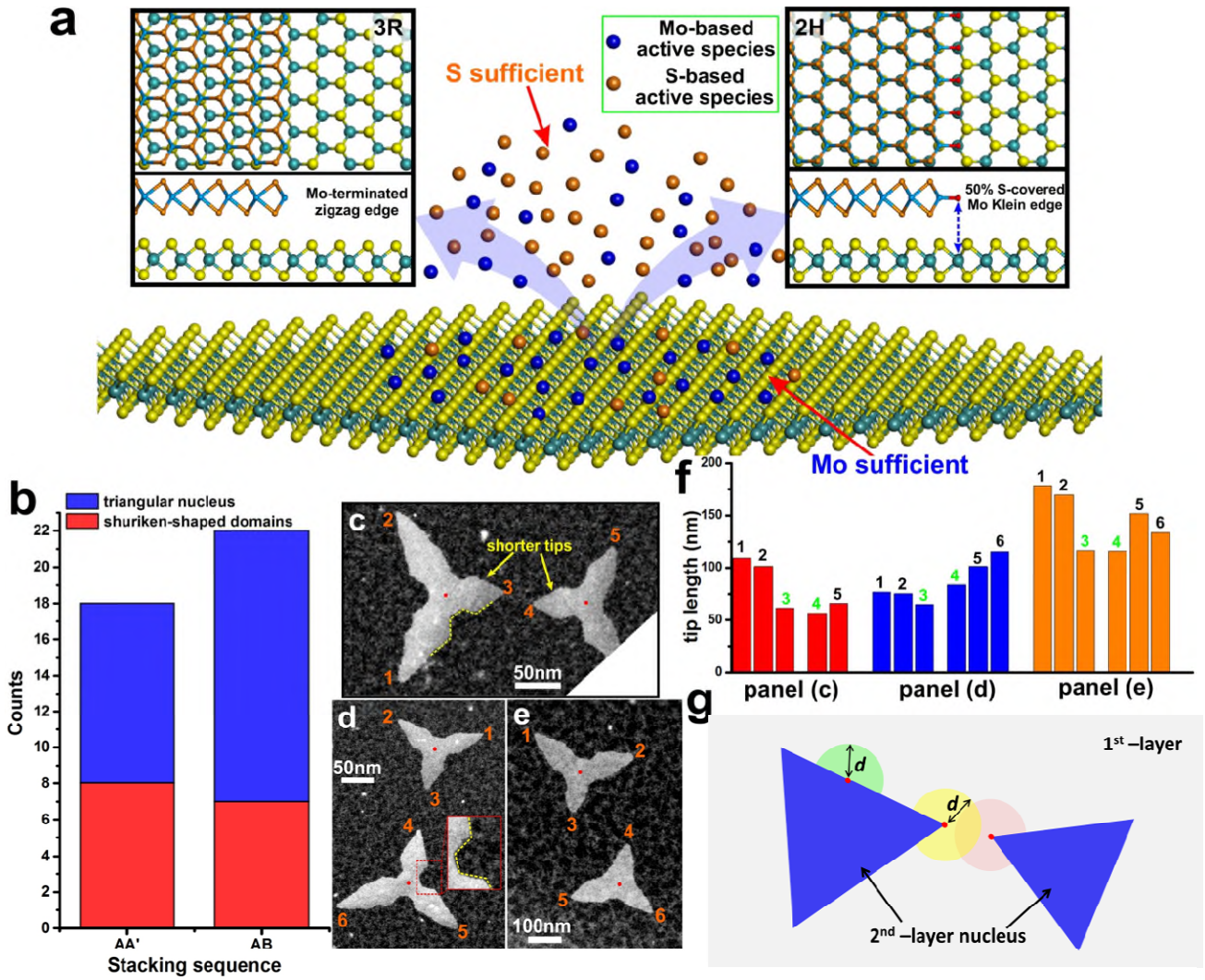

Figure 4. (a) Schematic illustration showing how a single layer MoS_2 substrate and different stacking sequences impact 2nd-layer step edge configurations. (b) Statistical plot showing the relative distribution of AA' and AB stacking sequences for bilayer MoS_2, considering both large shuriken-shaped domains and small triangular nuclei. (c-e) Low magnification HAADF-STEM images showing the domain geometry of three different pairs of shuriken-shaped MoS_2 second layers. The tips from two closely separated domains growing head to head are

shorter than the other tips. Insets show magnified images of the red-boxed region highlighting a special boundary morphology with several ~120° deflections. (f) Histograms of tip length variations in different domains in panels (c) to (e), showing a general phenomenon that head-to-head grown domain tips are shorter than their counterparts in the same domain. Different columns correspond to domain tips marked with the same number in panels (c) to (e). Red, blue and orange column colors indicate tips from (c), (d) and (e), respectively. (g) Schematic illustration of a potential formation mechanism of shuriken-shaped MoS_2 2^{nd}-layers on monolayer MoS_2, with the grey background indicating the 1^{st}-layer MoS_2. The green sector represents the region of precursor supplements for a point on the side of the 2^{nd}-layer nucleus, while the yellow and the red sectors represent the regions of precursor supplements for the point on the tip of two 2^{nd}-layer nuclei, respectively. All sectors have a radius of '*d*'.

In summary, we have shown that the mixed AA' and AB stacking of bilayer seeds of MoS_2 on larger MoS_2 monolayer single crystals have 60^o rotation on the lattice orientation. Mixed AA' and AB stacked bilayers are expected due to the small energy difference and subsequent thermodynamic distribution. The presence of two orientated lattice directions within the secondary domain nuclei will have impact on any final bilayer crystal produced when these merge, where the 60^o rotation will lead to an anti-phase boundary (inversion boundary). This indicates that creating pure single crystal bilayer by the merger of seed nuclei on the surface of a pre-existing monolayer TMD may be challenging. These insights gained here were only possible by using HAADF-STEM to provide elemental discrimination of Mo and S sites and show the Mo zig-zag orientated edges of both triangular shaped domains.

Methods

Synthesis and transfer of monolayer MoS_2

Epitaxially-grown three-pointed shuriken-shaped MoS_2 bilayers were synthesized using a similar approach to that previously reported.[49] Molybdenum trioxide (MoO_3, ≥99.5%, Sigma-Aldrich) and sulphur (S, ≥99.5%, Sigma-Aldrich) powder were used as precursors to grow bilayers on SiO_2/Si substrates (300 nm thick SiO_2) through a hydrogen-free chemical vapor deposition method (CVD) under atmospheric pressure. Two furnaces were used to give close independent control of temperature of the two precursors and the substrate. The heating temperature for S, MoO_3 and the SiO_2/Si substrate were ~ 180, ~300, and ~800 °C, respectively, with argon used as the carrier gas. To avoid the erosion of the MoO_3 powder by the S vapor, the MoO_3 powder was placed in an inner tube having a smaller diameter, which was then inserted into the larger 1-inch quartz tube. The S powder was loaded in the outer quartz tube. To increase the yield of bilayers, the growth time was increased by 5 minutes from the original recipe, thus increasing the nucleation density of second layers on monolayer MoS2. MoS2 was transferred onto the Si_3N_4 TEM grid (Agar Scientific AG21580) through a standard polymer-based method. The surface of the MoS_2/SiO_2/Si substrate was first spin-coated with a thin membrane of poly (methyl methacrylate) (PMMA) and then floated on the surface of a 1 mol/L potassium hydroxide (KOH) solution to remove SiO_2. After the PMMA/MoS_2 film was detached from the Si substrate, it was rinsed in deionized water several times and transferred to a holey Si_3N_4 grid. It was then air-dried and subsequently baked at 180 ^{0}C for 15 minutes. The grid was eventually submerged in acetone for 8 hours to dissolve the PMMA.

Scanning transmission electron microscopy and image processing

Room temperature HAADF-STEM imaging was performed on an aberration corrected JEOL ARM300CF STEM equipped with a JEOL ETA corrector[50] operated at an accelerating voltage of 80 kV located in the electron Physical Sciences Imaging Centre (ePSIC) at Diamond Light Source. The convergence semi-angle used was 24.6 mrad with a camera length of 20cm, which gave an annular recording range of 39-156mrad at the detector plane. The electron probe diameter was focused to

~52pm with a dwell time ranging from 10-20μs per pixel for imaging. The beam current was measured as 23 pA using a Pico ampere meter.

Images were processed using the ImageJ software. They were processed by applying a Gaussian blur (~1-2 pixels) for smoothing. SFor some grayscale HAADF-STEM images a fire false color LUT was applied to improve the visualisation. Atomic models were generated using the Accelrys Discovery Studio Visualizer. Multislice HAADF image simulation based on the corresponding atomic models were carried out using JEMS software with parameters corresponding to the imaging condition. For Figure 2e, Figure S1c and Figure S1f, key simulation parameters, including defocus spread, defocus and spherical aberration (Cs), were set to be 5.3nm, 16nm and 0.1mm, respectively, while for Figure 3e, these three parameters were 5.3nm, 14 nm and 0.08mm, respectively.

Conflict of Interest: The authors declare no competing financial interest.

Acknowledgements

JHW thanks the Royal Society for support. SW thanks the China Scholarship Council for support. AIK acknowledges EPSRC support under platform grant EP/K032518/1.

References

1 B. Radisavljevic, A. Radenovic, J. Brivio, V. Giacometti and A. Kis, *Nat. Nanotechnol.*, 2011, **6**, 147–150.

2 Q. H. Wang, K. Kalantar-Zadeh, A. Kis, J. N. Coleman and M. S. Strano, *Nat. Nanotechnol.*, 2012, **7**, 699–712.

3 R. Ganatra and Q. Zhang, *ACS Nano*, 2014, **8**, 4074–4099.

4 M. Amani, M. L. Chin, a. G. Birdwell, T. P. O'Regan, S. Najmaei, Z. Liu, P. M. Ajayan, J. Lou and M. Dubey, *Appl. Phys. Letts.*, 2013, **102**, 193107.

5 J. He, K. Hummer and C. Franchini, *Phys. Rev. B*, 2014, **89**, 075409.

6 A. Splendiani, L. Sun, Y. Zhang, T. Li, J. Kim, C.-Y. Chim, G. Galli and F. Wang, *Nano Letts.*, 2010, **10**, 1271–5.

7 H. Li, Q. Zhang, C. C. R. Yap, B. K. Tay, T. H. T. Edwin, A. Olivier and D. Baillargeat, *Adv. Funct. Mater.*, 2012, **22**, 1385–1390.

8 Y. Yu, S. Y. Huang, Y. Li, S. N. Steinmann, W. Yang and L. Cao, *Nano Letts.*, 2014, **14**, 553–558.

9 W. Bao, X. Cai, D. Kim, K. Sridhara and M. S. Fuhrer, *Appl. Phys. Letts.*, 2013, **102**, 042104.

10 G.-H. Lee, Y.-J. Yu, X. Cui, N. Petrone, C.-H. Lee, M. S. Choi, D.-Y. Lee, C. Lee, W. J. Yoo, K. Watanabe, T. Taniguchi, C. Nuckolls, P. Kim and J. Hone, *ACS Nano*, 2013, **7**, 7931–7936.

11 D. J. Late, Y. K. Huang, B. Liu, J. Acharya, S. N. Shirodkar, J. Luo, A. Yan, D. Charles, U. V. Waghmare, V. P. Dravid and C. N. R. Rao, *ACS Nano*, 2013, **7**, 4879–4891.

12 H. Li, Z. Yin, Q. He, H. Li, X. Huang, G. Lu, D. W. H. Fam, A. I. Y. Tok, Q. Zhang and H. Zhang, *Small*, 2012, **8**, 63–7.

13 A. Ramasubramaniam, D. Naveh and E. Towe, *Phys. Rev. B*, 2011, **84**, 205325.

14 Q. Liu, L. Li, Y. Li, Z. Gao, Z. Chen and J. Lu, *J. Phys. Chem. C*, 2012, **116**, 21556–21562.

15 T. Chu, H. Ilatikhameneh, G. Klimeck, R. Rahman and Z. Chen, *Nano Letts.*, 2015, **15**, 8000–8007.

16 R. Suzuki, M. Sakano, Y. J. Zhang, R. Akashi, D. Morikawa, A. Harasawa, K. Yaji, K. Kuroda, K. Miyamoto, T. Okuda, K. Ishizaka, R. Arita and Y. Iwasa, *Nat. Nanotechnol.*, 2014, **9**, 611–617.

17 J. Lee, K. F. Mak and J. Shan, *Nat. Nanotechnol.*, 2016, **11**, 421–425.

18 J. Yan, J. Xia, X. Wang, L. Liu, J. L. Kuo, B. K. Tay, S. Chen, W. Zhou, Z. Liu and Z. X. Shen, *Nano Letts.*, 2015, **15**, 8155–8161.

19 K. Liu, L. Zhang, T. Cao, C. Jin, D. Qiu, Q. Zhou, A. Zettl, P. Yang, S. G. Louie and F. Wang, *Nat. Commun.*, 2014, **5**, 4966.

20 A. Yacoby, *Nat. Phys.*, 2011, **7**, 925–926.

21 I. Song, C. Park and H. C. Choi, *RSC Adv.*, 2015, **5**, 7495–7514.

22 A. M. van der Zande, J. Kunstmann, A. Chernikov, D. a Chenet, Y. You, X. Zhang, P. Y. Huang, T. C. Berkelbach, L. Wang, F. Zhang, M. S. Hybertsen, D. a Muller, D. R. Reichman, T. F. Heinz and J. C. Hone, *Nano Letts.*, 2014.

23 P. C. Yeh, W. Jin, N. Zaki, J. Kunstmann, D. Chenet, G. Arefe, J. T. Sadowski, J. I. Dadap, P. Sutter, J. Hone and R. M. Osgood, *Nano Letts.*, 2016, **16**, 953–959.

24 K. Kang, S. Xie, L. Huang, Y. Han, P. Y. Huang, K. F. Mak, C.-J. Kim, D. Muller and J. Park, *Nature*, 2015, **520**, 656–660.

25 S. Wang, M. Pacios, H. Bhaskaran and J. H. Warner, *Nanotechnology*, 2016, **27**, 85604–85611.

26 J. Zhang, H. Yu, W. Chen, X. Tian, D. Liu, M. Cheng, G. Xie, W. Yang, R. Yang, X. Bai, D. Shi and G. Zhang, *ACS Nano*, 2014, **8**, 6024–6030.

27 V. Senthilkumar, L. Tam, Y. Kim and Y. Sim, *Nano Res.*, 2014, **7**, 1759–1768.

28 Y. W. Son, M. L. Cohen and S. G. Louie, *Phys. Rev. Letts.*, 2006, **97**, 216803.

29 Y.-W. Son, M. L. Cohen and S. G. Louie, *Nature*, 2006, **444**, 347–349.

30 Z. Luo, S. Kim, N. Kawamoto, A. M. Rappe and a T. C. Johnson, *ACS Nano*, 2011, **5**, 9154–60.

31 S. Wang, Y. Rong, Y. Fan, M. Pacios, H. Bhaskaran, K. He and J. H. Warner, *Chem. Mater.*, 2014, **26**, 6371–6379.

32 E. Erdogan, I. H. Popov, A. N. Enyashin and G. Seifert, *Eur. Phys. J. B*, 2012, **85**, 33–36.

33 C. Ataca, H. Şahin, E. Aktürk and S. Ciraci, *J. Phys. Chem. C*, 2011, **115**, 3934–3941.

34 B. Hinnemann, P. G. Moses, J. Bonde, K. P. Jorgensen, J. H. Nielsen, S. Horch, I. Chorkendorff and J. K. Nørskov, *J. Am. Chem. Soc.*, 2005, **127**, 5308–5309.

35 Y. Li, Z. Zhou, S. Zhang and Z. Chen, *J. Am. Chem. Soc.*, 2008, **130**, 16739–44.

36 K. He, G.-D. Lee, A. W. Robertson, E. Yoon and J. H. Warner, *Nat. Commun.*, 2014, **5**, 3040.

37 K. He, A. W. Robertson, S. Lee, E. Yoon, G. Lee and J. H. Warner, *ACS Nano*, 2014, **8**, 12272–12279.

38 K. Kim, S. Coh, C. Kisielowski, M. F. Crommie, S. G. Louie, M. L. Cohen and A. Zettl, *Nat. Commun.*, 2013, **4**, 2723.

39 W. Zhou, X. Zou, S. Najmaei, Z. Liu, Y. Shi, J. Kong, J. Lou, P. M. Ajayan, B. I. Yakobson and J.-C. Idrobo, *Nano Letts.*, 2013, **13**, 2615–2622.

40 K. Suenaga and M. Koshino, *Nature*, 2010, **468**, 1088–1090.

41 O. L. Krivanek, M. F. Chisholm, V. Nicolosi, T. J. Pennycook, G. J. Corbin, N. Dellby, M. F. Murfitt, C. S. Own, Z. S. Szilagyi, M. P. Oxley, S. T. Pantelides and S. J. Pennycook, *Nature*, 2010, **464**, 571–574.

42 S. Wang, Z. Qin, G. S. Jung, F. J. Martin-Martinez, K. Zhang, M. J. Buehler and J. H. Warner, *ACS Nano*, 2016, **10**, 9831–9839.

43 G. Constantinescu, A. Kuc and T. Heine, *Phys. Rev. Letts.*, 2013, **111**, 036104.

44 A. M. van der Zande, P. Y. Huang, D. A. Chenet, T. C. Berkelbach, Y. You, G.-H. Lee, T. F. Heinz, D. R. Reichman, D. A. Muller and J. C. Hone, *Nat. Mater.*, 2013, **12**, 554–561.

45 H. Schweiger, P. Raybaud, G. Kresse and H. Toulhoat, *J. Catal.*, 2002, **207**, 76–87.

46 A. Govind Rajan, J. H. Warner, D. Blankschtein and M. S. Strano, *ACS Nano*, 2016, **10**, 4330–4344.

47 D. J. Woodland and E. Mack Jr., *J. Am. Chem. Soc.*, 1933, **55**, 3149–3161.

48 Y.-H. Lee, X.-Q. Zhang, W. Zhang, M.-T. Chang, C.-T. Lin, K.-D. Chang, Y.-C. Yu, J. T.-W. Wang, C.-S. Chang, L.-J. Li and T.-W. Lin, *Adv. Mater.*, 2012, **24**, 2320–5.

49 S. Wang, X. Wang and J. H. Warner, *ACS Nano*, 2015, **9**, 5246–5254.

50 F. Hosokawa, H. Sawada, Y. Kondo, K. Takayanagi and K. Suenaga, *Microscopy*, 2013, **62**, 23–41

TOC graphic